INTERNATIONAL JOURNAL FOR NUMERICAL METHODS IN FLUIDS, VOL. 17, 825–837 (1993)

EXTENSION OF MULTIGRID METHODOLOGY TO SUPERSONIC/HYPERSONIC 3-D VISCOUS FLOWS

VEER N. VATSA

NASA Langley Research Center, Hampton, VA 23665, U.S.A.

ELI TURKEL*

I CASE and Tel-Aviv University, Israel

AND

J. S. ABOLHASSANI

Computer Sciences Corporation, Hampton, VA, U.S.A.

SUMMARY

A multigrid acceleration technique developed for solving the three-dimensional Navier–Stokes equations for subsonic/transonic flows has been extended to supersonic/hypersonic flows. An explicit multistage Runge–Kutta type of time-stepping scheme is used as the basic algorithm in conjunction with the multigrid scheme. Solutions have been obtained for a blunt conical frustum at Mach 6 to demonstrate the applicability of the multigrid scheme to high-speed flows. Computations have also been performed for a generic High-Speed Civil Transport configuration designed to cruise at Mach 3. These solutions demonstrate both the efficiency and accuracy of the present scheme for computing high-speed viscous flows over configurations of practical interest.

KEY WORDS Multigrid Supersonic Hypersonic Viscous

INTRODUCTION

During the last decade or so, significant progress has been made in the field of Computational Fluid Dynamics (CFD) to have an impact on the design and analysis of aerodynamic configurations. Solutions of the Euler (inviscid) equations for essentially complete aircraft configurations[1–4] and the solutions of the Navier–Stokes equations for high Reynolds number, viscous, transonic flows over aircraft components are now available in the open literature.[5–9] It is noteworthy that most of the efficient numerical schemes for solving aerodynamic flows rely on multigrid acceleration technique[2,8,9] to enhance the convergence rate. The multigrid-based schemes have the desirable property that the number of iterations required to achieve a steady-state solution is nearly independent of the mesh size for a given class of problems. Thus one can achieve essentially grid-converged, steady-state solutions, even for the numerically demanding

* This research was supported by the National Aeronautics and Space Administration under NASA Contract No. NAS1-18605 while the author was in residence at the Institute for Computer Applications in Science and Engineering (ICASE), NASA Langley Research Center, Hampton, VA 23665.

0271–2091/93/220825–13$11.50

Received 22 July 1991
Revised 22 April 1992

problem of high Reynolds number, transonic, viscous flow over realistic aerodynamic configurations with a reasonable amount of computer resources.[9]

Despite the progress achieved in solving transonic flows, the development of CFD methods for supersonic/hypersonic flows seems to be lagging behind at the present time. With the current interest in high-speed vehicles such as the High-Speed Civil Transport (HSCT) and the National Aero-space Plane (NASP), it is imperative that efficient computational algorithms be developed for high-speed flow regimes. In Reference 10 it is shown that central difference schemes can be used for solving inviscid, high-speed flows in conjunction with standard multigrid acceleration techniques that were originally developed for low-speed flows. Difficulties that some researchers have had with multigrid for high speed flows are due mainly to the non-smoothness of the flux limiters rather than the deficiencies in the multigrid strategy. Nevertheless, we stress that there is very little theoretical work in the use of multigrid for supersonic and hypersonic flows. In this paper, we demonstrate further progress in the use of a multigrid based central difference scheme. We present several results for three dimensional viscous problems that demonstrate the accuracy and efficiency of the proposed method for high-speed flows.

GOVERNING EQUATIONS AND NUMERICAL METHODS

The basic equations under consideration here are the unsteady Navier–Stokes equations. These are specialized to a body-fitted coordinate system (ξ, η, ζ), where ξ, η, and ζ represent the streamwise, normal, and spanwise co-ordinates, respectively. The η co-ordinate lines are nearly orthogonal to the solid surface. Since the dominant viscous effects for high-Reynolds-number turbulent flows arise from viscous diffusion normal to the body surface, a thin-layer assumption is employed here by retaining only the viscous diffusion terms in the η-direction. These equations can be written in the conservation law form as

$$\frac{\partial}{\partial t}(J^{-1}U)+\frac{\partial F}{\partial \xi}+\frac{\partial G}{\partial \eta}+\frac{\partial H}{\partial \zeta}=\frac{\partial G_v}{\partial \eta} \tag{1}$$

where the dependent variable vector U is given by the relation

$$U=\begin{Bmatrix} \rho \\ \rho u \\ \rho v \\ \rho w \\ \rho E \end{Bmatrix} \tag{2}$$

In equation (1), F, G, G_v and H are the flux vectors, and J is the Jacobian of the transformation. The complete forms of these quantities are readily available in Reference 9.

A pseudo time-stepping scheme based on a Runge–Kutta scheme[11,12] is used for integrating the time-dependent equations to steady state and as a smoother in the multigrid scheme. For convenience, let us first write the discretized form of the governing equations in the following operator notation:

$$\frac{\mathrm{d}}{\mathrm{d}t}(J^{-1}U)+Q(U)-D(U)=0 \tag{3}$$

where Q contains all the convective and viscous fluxes and D represents the artificial dissipative fluxes.

Since our primary interest here is to obtain solutions for viscous flows via the Navier–Stokes equations, both the diffusion and the convective terms are important in contrast with the Euler equations where convective terms are dominant. Therefore, it is preferable to employ a scheme that has a larger stability bound along the real axis in addition to good stability properties along the imaginary axis. Based on the Fourier stability analysis of a one-dimensional model problem, the five-stage Runge–Kutta scheme proposed by Jameson,[13] with 3 evaluations of the dissipative operator at the first, third, and fifth stages, appears to be very attractive and is employed in the present work. The convergence to steady state is enhanced via the use of local time-stepping and implicit residual smoothing techniques,[11,12] with the coefficients of the residual smoothing computed in the manner described by Vatsa and Wedan.[9]

ARTIFICIAL DISSIPATION MODEL

The basic artificial dissipation model used in this study is patterned after the work of Jameson, Schmidt and Turkel[11] and of Jameson and Baker[12] for 2-D and 3-D Euler equations respectively, and modified later by Vatsa and Wedan[9] for 3-D Navier–Stokes equations. In order to discuss the modifications required for supersonic/hypersonic flows, let us first examine the dissipation terms in the i-direction:

$$\frac{d_{i+1/2,j,k}}{\lambda_{i+1/2,j,k}}=\varepsilon^{(2)}_{i+1/2,j,k}(W_{i+1,j,k}-W_{i,j,k})-\varepsilon^{(4)}_{i+1/2,j,k}(W_{i+2,j,k}-3W_{i+1,j,k}+3W_{i,j,k}-W_{i-1,j,k}). \quad (4)$$

In the above expression, $\lambda_{i+1/2,j,k}$ is the modified eigenvalue scaling factor[9] and the coefficients $\varepsilon^{(2)}$ and $\varepsilon^{(4)}$ are related to the pressure gradient as follows:

$$\begin{aligned}\varepsilon^{(2)}_{i+1/2,j,k}&=\kappa^{(2)}\max(\nu_{i+1},\nu_i)\\ \varepsilon^{(4)}_{i+1/2,j,k}&=\max\{0,(\kappa^{(4)}-\varepsilon^{(2)}_{i+1/2,j,k})\}\end{aligned} \quad (5)$$

where the coefficients $\kappa^{(2)}$ and $\kappa^{(4)}$ are set equal to 1/2 and 1/64, respectively. The term ν depends on the pressure gradient and is modified to give a TVD variation of the shock switch[14] in the following manner:

$$\nu_i=\frac{|p_{i+1,j,k}-2p_{i,j,k}+p_{i-1,j,k}|}{(1-\omega)(|p_{i+1,j,k}-p_{i,j,k}|+|p_{i,j,k}-p_{i-1,j,k}|)+\omega(p_{i+1,j,k}+2p_{i,j,k}+p_{i-1,j,k})}. \quad (6)$$

Note that by setting $\omega=1$, we can recover the shock switch that has been used in earlier studies for computing transonic flows.[9,11-13] For supersonic and hypersonic flows, where shocks are much stronger, we use $\omega=1/2$. The expressions for the dissipation terms in the j and k directions are derived in a similar manner.

In Reference 15 it is shown that for transonic flows one should choose $\omega\sim 1$, since smaller values of ω result in excessively smeared shocks. It is possible to choose ω adaptively depending on the shock strength so that an appropriate value of ω is used for the entire Mach number range. For the hypersonic flows considered in this study, such a strategy was found to have no clear advantage over a constant ω of 1/2.

EVALUATION OF TIME STEP

It is very important to estimate the allowable time-step as accurately as possible in order to construct a robust time-stepping scheme. Failure to do so generally creates difficulties when the

scheme is applied to different flow problems with widely varying test conditions and grid-densities. An attempt is made here to derive the expressions for allowable time step for the present scheme from stability considerations. For convenience, let us start with the Navier–Stokes equations written in non-conservative form:

$$\frac{\partial U}{\partial t}+A\frac{\partial U}{\partial x}+B\frac{\partial U}{\partial y}+C\frac{\partial U}{\partial z}=D\frac{\partial^2 U}{\partial x^2}+E\frac{\partial^2 U}{\partial y^2}+F\frac{\partial^2 U}{\partial z^2}+G_{xy}\frac{\partial^2 U}{\partial x\partial y}+G_{yz}\frac{\partial^2 U}{\partial y\partial z}+G_{zx}\frac{\partial^2 U}{\partial z\partial x} \tag{7}$$

where U is the velocity vector and $A, B, \cdots G_{zx}$ are the coefficient matrices, their full form being available in Reference 16.

Transforming these equations to the body-fitted curvilinear coordinate system ξ, η and ζ, and making the thin-layer assumption, one gets

$$\frac{\partial U}{\partial t}+[A\xi_x+B\xi_y+C\xi_z]\frac{\partial U}{\partial \xi}+[A\eta_x+B\eta_y+C\eta_z]\frac{\partial U}{\partial \eta}+[A\zeta_x+B\zeta_y+C\zeta_z]\frac{\partial U}{\partial \zeta}$$

$$=[D\eta_x^2+E\eta_y^2+F\eta_z^2+G_{xy}\eta_x\eta_y+G_{yz}\eta_y\eta_z+G_{zx}\eta_z\eta_x]\frac{\partial^2 U}{\partial \eta^2} \tag{8}$$

In general it is very difficult to derive an exact expression for the time step Δt, since the coefficient matrices are non-symmetric. Abarbanel and Gottlieb[16] have delineated a procedure to symmetrize all of these coefficient matrices simultaneously. Taking advantage of their work, and the property that the norm of a symmetric matrix equals its spectral radius, one can find an upper bound on Δt in the following manner:

$$\frac{1}{\Delta t}\geqslant\frac{1}{\Delta t_\xi}+\frac{1}{\Delta t_\eta}+\frac{1}{\Delta t_\zeta}+\frac{1}{\Delta t_{\text{diff}}} \tag{9}$$

where, the first three terms on the right-hand side arise due to the convective terms and the last term is due to diffusion terms. Setting the bounds of these components of Δt equal to their respective spectral radii, we arrive at the following expressions for the convective terms:

$$\frac{1}{\Delta t_\xi}\geqslant\lambda_\xi=|u\xi_x+v\xi_y+w\xi_z|+c\sqrt{(\xi_x^2+\xi_y^2+\xi_z^2)} \tag{10}$$

$$\frac{1}{\Delta t_\eta}\geqslant\lambda_\eta=|u\eta_x+v\eta_y+w\eta_z|+c\sqrt{(\eta_x^2+\eta_y^2+\eta_z^2)} \tag{11}$$

$$\frac{1}{\Delta t_\zeta}\geqslant\lambda_\zeta=|u\zeta_x+v\zeta_y+w\zeta_z|+c\sqrt{(\zeta_x^2+\zeta_y^2+\zeta_z^2)} \tag{12}$$

where c is the speed of sound. The diffusion limit on the time step is obtained in a similar manner and is given by the relation

$$\frac{1}{\Delta t_{\text{diff}}}\geqslant\lambda_{\text{diff}}=\frac{\mu}{\rho}\left[(\eta_x^2+\eta_y^2+\eta_z^2)\left\{\max\left(\frac{4}{3},\frac{\gamma}{Pr}\right)\right\}+\frac{1}{3}\{|\eta_x\eta_y|+|\eta_y\eta_z|+|\eta_z\eta_x|\}\right] \tag{13}$$

For viscous flow problems, the most restrictive time step is in the boundary layer region near a solid surface, where Δt_η and Δt_{diff} are the most critical terms in determining the actual value of Δt. In order to get better understanding of the viscous time step limit, let us normalize the flow variables so that $p_{\text{ref}}=p_\infty$, $\rho_{\text{ref}}=\rho_\infty$, $T_{\text{ref}}=T_\infty$, $u_{\text{ref}}=\sqrt{(\gamma p_\infty/\rho_\infty)}$. For the thin-layer approximation, one obtains the following simplified expressions for the diffusion and convection limits near

the wall,

$$\lambda_{\text{diff}} \sim \frac{M_\infty p(\eta_x^2+\eta_y^2+\eta_z^2)}{\rho^2 PrRe} \tag{14}$$

$$\lambda_\eta \sim \frac{p^{1/2}}{\rho^{1/2}}\sqrt{(\eta_x^2+\eta_y^2+\eta_z^2)} \tag{15}$$

We express these quantities in terms of far field data by using the normal shock relations. In the vicinity of strong shocks, $p \to 6M_\infty^2/5$, $\rho \to 6$ as $M_\infty \to \infty$. Therefore,

$$\lambda_{\text{diff}} \sim \frac{M_\infty^3(\eta_x^2+\eta_y^2+\eta_z^2)}{PrRe} \tag{16}$$

$$\lambda_\eta \sim M_\infty\sqrt{(\eta_x^2+\eta_y^2+\eta_z^2)} \tag{17}$$

For the thin-layer approximation one obtains the following simplified expression for the ratio of diffusion limit to the convection limit near the wall:

$$\frac{\lambda_{\text{diff}}}{\lambda_\eta} \sim \frac{M_\infty^2}{RePr}\sqrt{(\eta_x^2+\eta_y^2+\eta_z^2)} \tag{18}$$

Thus for fixed Reynolds number $\lambda_{\text{diff}}/\lambda_\eta \sim M_\infty^2$ on a given grid. This indicates that the diffusion time limit in the thin viscous layer near wall becomes more important than the convection limit as the Mach number is increased. It must also be realized that a finer mesh spacing is required as the Reynolds number is increased for a given Mach number flow, which makes the diffusion limit even more dominant (equations (16)–(18)).

MULTIGRID ACCELERATION TECHNIQUE

The convergence acceleration due to the use of multigrid techniques has been demonstrated for both inviscid and viscous flows[8,9,13] in the transonic flow regimes. In the current application, the Full Approximation Storage (FAS) scheme of Brandt[17] is used in conjunction with the multigrid strategy devised by Jameson[13] for the solution of the Euler equations. The extension of the scheme of Reference 13 to the three-dimensional thin-layer Navier–Stokes equations for transonic flows described by Vatsa and Wedan[9] is used as a starting point for this work. A 5-stage Runge–Kutta scheme with coefficients selected to provide optimum damping of the high-frequency errors is employed. The restriction operator used to transfer the solution to a coarser grid is a volume-weighted average of the eight surrounding cell-centered values. The forcing function for a cell on the coarse grid is obtained by simply summing the residuals of its constituent fine-grid cells. The corrections are transferred from the coarse grid back to the fine grid (or prolonged) by simple trilinear interpolation in computational space. On highly stretched or non-uniform grids, this prolongation operator can introduce high-frequency errors back to the fine grid, causing degradation of the convergence rate. To prevent this, the coarse-grid corrections were processed through an implicit residual smoothing operator before adding to the fine-grid corrections. Whereas the smoothing of the coarse-grid corrections was certainly helpful for transonic flow calculations, it was found to be essential for obtaining converged solutions for higher speed flows.

The solutions presented in this paper were obtained using a *W*-cycle, in which governing equations are solved only in the restriction step. The *W*-cycle resulted in approximately a 25 per

cent improvement in computational time compared to a standard V-cycle for achieving comparable convergence levels of the residuals. In addition, global properties such as lift and drag, develop more rapidly with the W-cycle, since more time is spent on the coarser grids. It was also found helpful to run more cycles on coarser grid levels for supersonic and hypersonic flows in order to better establish and precondition the flowfield before starting computations on the finest mesh in the Full Multigrid (FMG) cycle.

The variable-coefficient residual smoothings were applied on all grid levels of the multigrid cycle. On the finest grid, the blend of second- and fourth-difference artificial dissipation discussed previously was employed. For the coarser grids, a fixed coefficient second-difference dissipation model has been found adequate for transonic flow computations.[3] However, the coarse-grid dissipation model had to be modified via a pressure gradient based TVD switch (see equations (5) and (6)) to improve the convergence rate of the present scheme in supersonic and hypersonic flow regimes.

RESULTS AND DISCUSSION

Two test cases covering supersonic to low hypersonic speed regimes are chosen for testing the multigrid Navier–Stokes code described in the preceding paragraphs. The accuracy of the computed solutions is assessed via comparisons with available experimental data. In the present investigation, C–O type grids are employed. The computational grids are generated so as to cluster points in the appropriate regions to resolve sharp gradients present therein. In addition, significant grid clustering is used in the thin region adjacent to the solid surface in order to resolve the thin shear layers present in high Reynolds number turbulent flows.

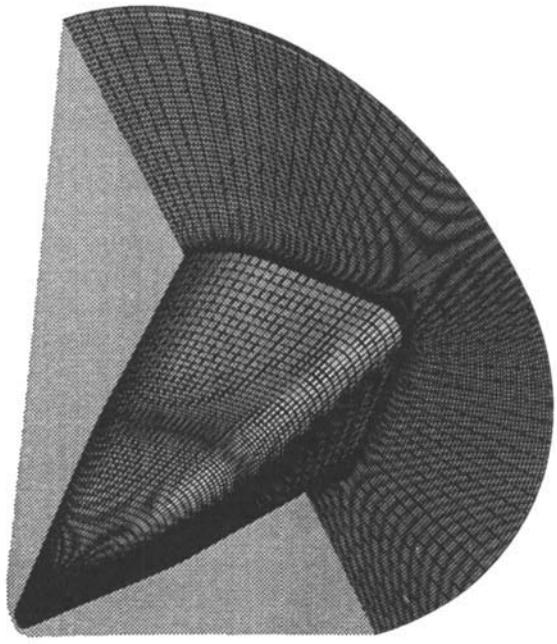

Figure 1. Partial view of grid for conical frustum

Conical frustum entry configuration

The first test case used for this study is a simple aerodynamic shape designed for entry at Mach 6. The configuration consists of a modified conical frustum[18] and is shown in Figure 1, along with the downstream and symmetry planes. This configuration evolved through a conceptual study for the design of a vehicle to accommodate an 8-person crew, which could sustain a supersonic/hypersonic reentry and be capable of landing as a paraglider.[18] A wind tunnel model was tested at $M_\infty = 6{\cdot}0$ and Reynolds number of $0{\cdot}8 \times 10^6$ based on the model length. The Navier–Stokes calculations were performed on a grid consisting of $161 \times 65 \times 29$ mesh points. The lift- and drag-coefficient data from the wind-tunnel tests are available for up to an angle of attack (α) of 12°. The Navier–Stokes solutions spanning this entire angle-of-attack range have been obtained to assess the performance of the current scheme over such a large range of test conditions.

The convergence history in terms of the residual error of the continuity equation and the lift coefficient, C_l for the $\alpha = 6°$ case are shown in Figure 2 as a function of work-units, where a work unit represents the computational effort required for one fine-mesh iteration. A total of 400 iterations (620 work-units) were performed on the fine grid which resulted in approximately seven orders of reduction in the residual. The lift and drag coefficients for this case converged to within 0·1 per cent of their final values in less than 50 fine-grid iterations. The convergence histories for this series of test cases are similar to the $\alpha = 6°$ case shown in Figure 2 except for the case of $\alpha = 12°$, for which the residual started oscillating after dropping approximately five orders, possibly due to slight unsteadiness.

The computed lift and drag coefficients for $\alpha = 0$–$12°$ shown in Figure 3, are found to be in excellent agreement with the experimental data over the complete range of α. Thus, not only does the present scheme have good convergence properties for these test conditions, but in addition it produces accurate solutions that are in good quantitative agreement with the experimental data.

A better understanding of the overall flow field is obtained by examining Figure 4, where the pressure contours for the $\alpha = 6°$ case are shown on the symmetry and downstream planes, in addition to the body surface. One can clearly observe the nearly conical growth of the shock surface in the streamwise direction. In the crossflow direction, the distance between the shock and the body surface goes through a minimum near the tip and then increases towards both the windward and the leeward planes of symmetry.

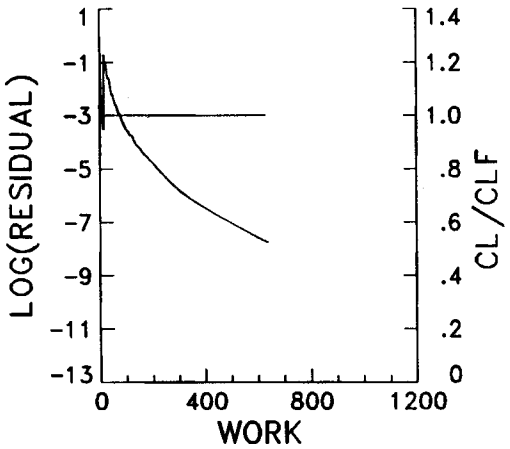

Figure 2. Convergence history for conical frustum on $161 \times 65 \times 29$ grid, $M_\infty = 6{\cdot}0$, $\alpha = 6°$, $Re_l = 0{\cdot}8 \times 10^6$

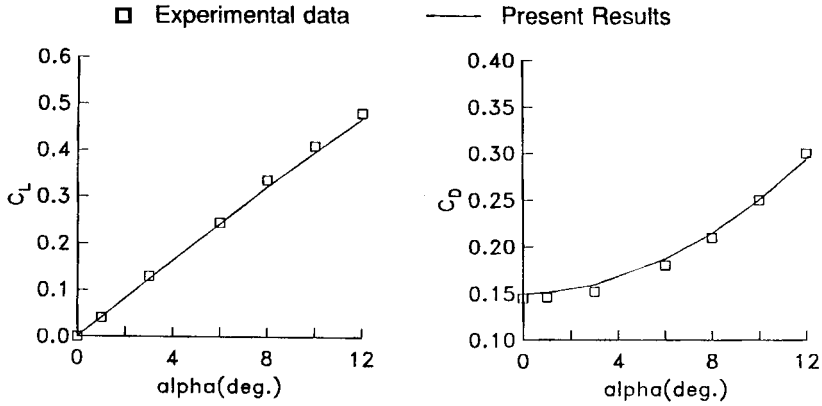

Figure 3. Comparison of force coefficient for conical frustum, $M_\infty = 6{\cdot}0$, $Re_l = 0{\cdot}8 \times 10^6$

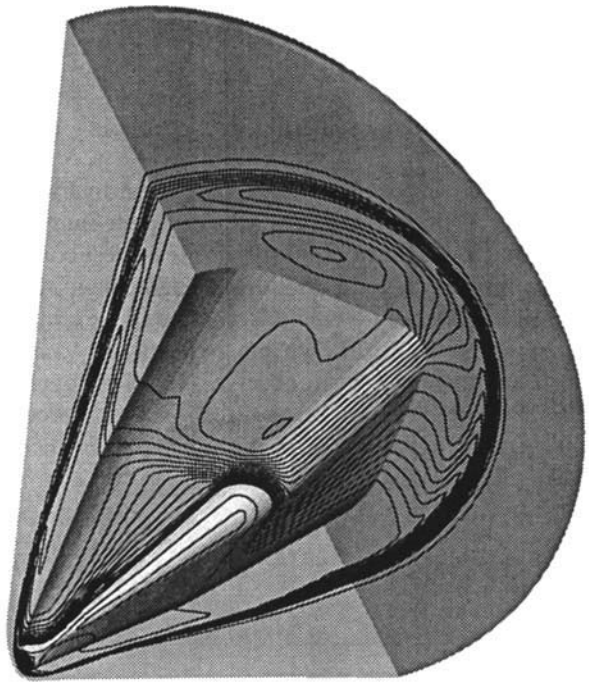

Figure 4. Pressure contours for conical frustum, $M_\infty = 6{\cdot}0$, $\alpha = 6°$, $Re_l = 0{\cdot}8 \times 10^6$

High-speed civil transport

The next test case considered here is that of the flow over a generic High-Speed Civil Transport (HSCT) configuration designed to cruise at a Mach number, $M_\infty = 3{\cdot}0$. The conceptual development and geometric details of this highly blended wing/body configuration are available in Reference 19. A wind-tunnel model representative of this vehicle was tested over a large angle-of-attack range for several Mach numbers, and the experimental data from this study have

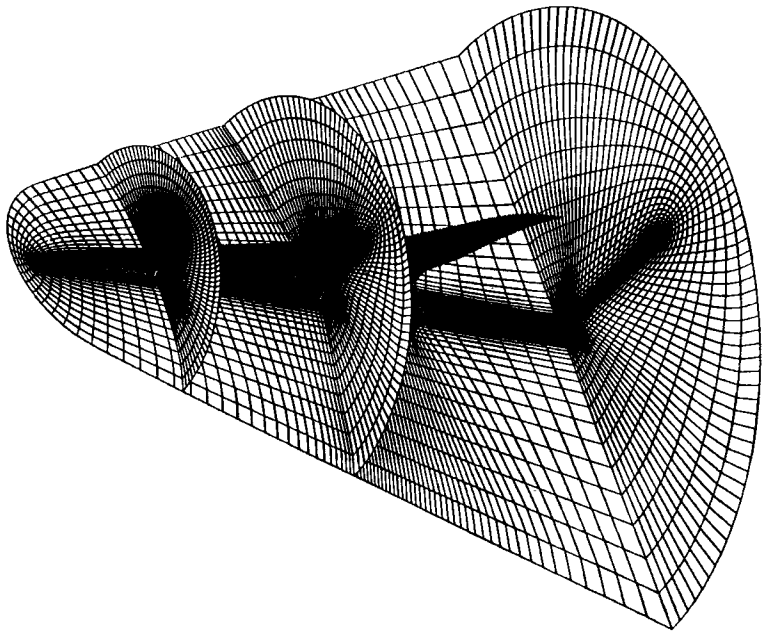

Figure 5. Partial view of grid for HSCT

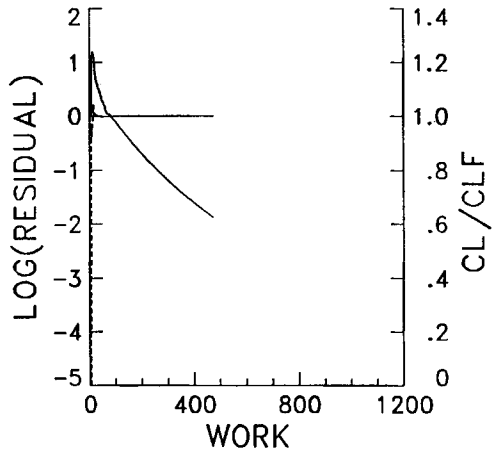

Figure 6. Convergence history for HSCT on $145 \times 65 \times 73$ grid, $M_\infty = 3{\cdot}0$, $\alpha = 5°$, $Re_l = 6{\cdot}3 \times 10^6$

been documented by Covell *et al.*[20] In the present study, we will concentrate on the $M_\infty = 3{\cdot}0$ case, which was the design cruise Mach number for this configuration. The corresponding Reynolds number based on model length was $6{\cdot}3 \times 10^6$.

A grid consisting of $145 \times 65 \times 73$ nodes was generated for the Navier–Stokes calculations. A partial view of the mesh on the symmetry plane and several streamwise cuts is displayed in Figure 5. The outer boundaries of the grid were placed so as to contain the shock emanating from the leading-edge within the computational domain. Grid clustering in the tip, leading and trailing-edges are used to accurately resolve the flow in high-gradient regions.

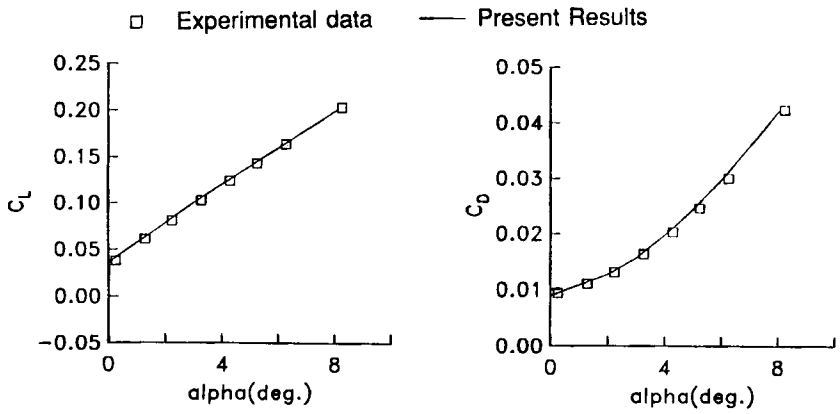

Figure 7. Comparison of force coefficients for HSCT, $M_\infty = 3{\cdot}0$, $Re_l = 6{\cdot}3 \times 10^6$

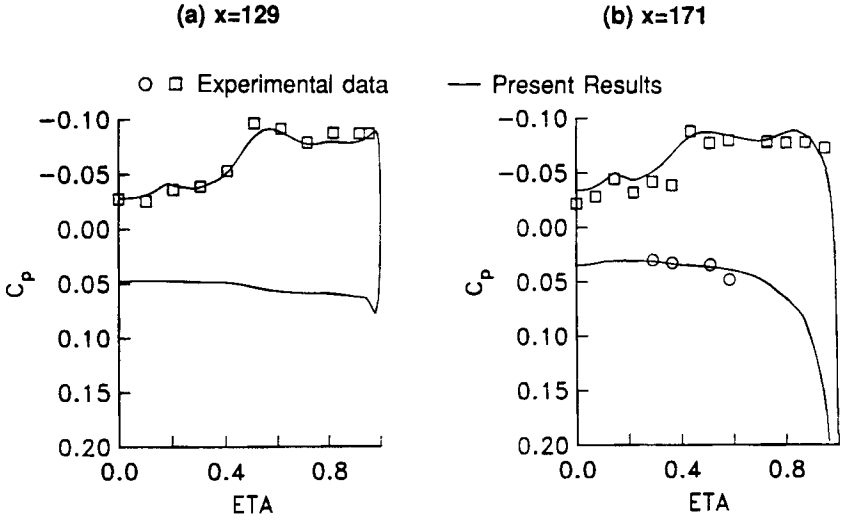

Figure 8. Comparison of surface pressure distributions for HSCT, $M_\infty = 3{\cdot}0$, $\alpha = 5°$, $Re_l = 6{\cdot}3 \times 10^6$

The convergence histories for the lift and residual of the continuity equation for the $\alpha = 5°$ are shown in Figure 6, which shows a reduction of three orders in the residual after 300 fine grid iterations (470 work units). The lift for this case converged after about 50 iterations. The convergence histories for the entire angle-of-attack range considered here ($\alpha = 0$–$8°$) are very similar to this case. The integrated lift and drag coefficients are compared with the experimental data of Reference 20 over the complete range of angle of attack in Figure 7. It is clear from this figure that the computed results are in very good agreement with the experimental data. This is very encouraging especially for drag prediction, since viscous drag, which is difficult to predict accurately, constitutes a significant part of the total drag for this configuration at Mach 3.

Next we examine the detailed surface pressure distributions for this vehicle. For this purpose, we concentrate again on the $\alpha = 5°$ case for which experimental pressure data are available at selected streamwise and spanwise stations. Since the computational grid does not follow the cuts

along which experimental data was acquired, the computed pressure distributions had to be interpolated for a meaningful comparison. The interpolated solutions at two x-locations are compared with the experimental data in Figure 8. For the station $x = 129$, experimental pressures are available only on the upper surface, whereas both upper- and lower-surface pressures are available at the $x = 171$ station. The agreement with the measured pressure data at both of these stations is quite good. It is noted that the computed solutions predict the correct variation in pressure even in the vortex-dominated flow near the wing-tip region. Similar comparisons have also been obtained at $\alpha = 1°$ and $\alpha = 3°$; however these results are not shown here for conciseness.

Whereas the global force coefficients and surface pressure comparisons are helpful in quantitative validation of a prediction method, these flow properties are inadequate for understanding the true three-dimensional nature of the flow problem, such as the development of vortical-flow regions off the wing-tips. Following the lead of Reference 21, an attempt is made here to visualize the vortical flow by plotting the density contours at fixed x-locations. This is done in Figure 9 for $x = 129$ and $x = 171$, the same stations for which the surface pressure distributions were examined. The experimental laser sheet photographs, that are used routinely for visualizing shock and

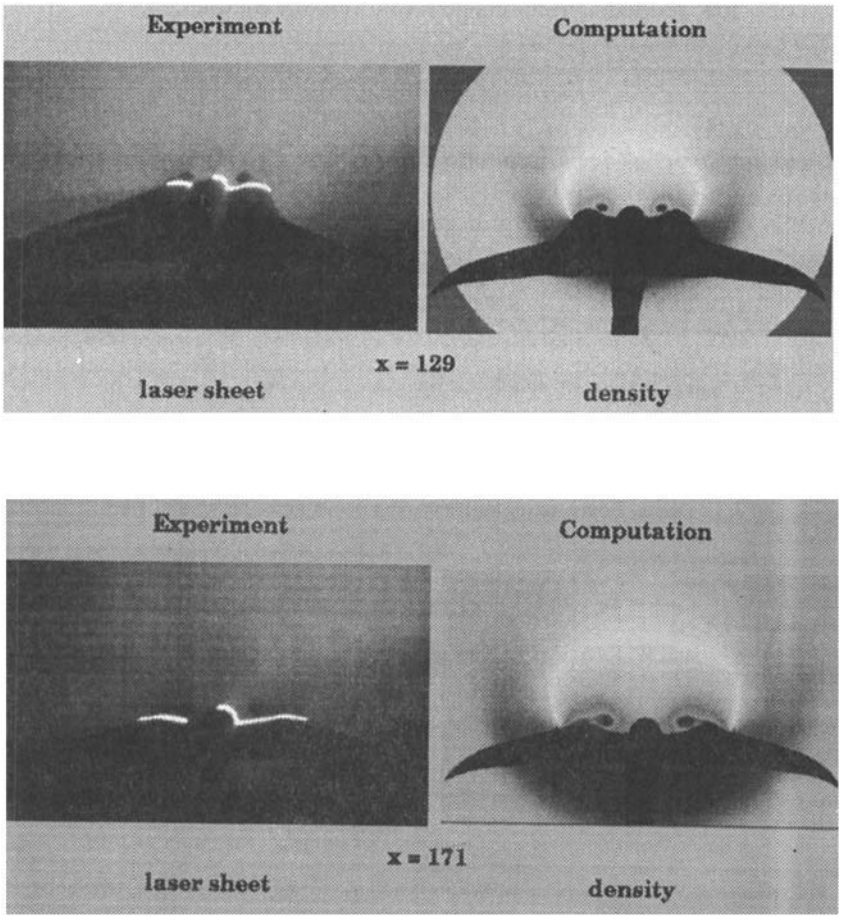

Figure 9. Flow-field visualization for HSCT, $M_\infty = 3{\cdot}0$, $Re_l = 6{\cdot}3 \times 10^6$

vortex formations are also shown in Figure 9 at the corresponding stations. The core of the vortex forming between the wing-tip and the fuselage and its feeding sheets are the most dominant flow structure visible in these figures. After a careful examination of these results, the following observations can be made. First, the core of the vortex is predicted to grow in size and lift off farther away from the surface as one moves downstream. Secondly, the overall shape and size of the vortex predicted by the Navier–Stokes calculations are in reasonably good agreement with the laser-sheet data.

CONCLUDING REMARKS

A multigrid acceleration technique developed originally for transonic flows has been extended to solve the three-dimensional Navier–Stokes equations for supersonic and hypersonic viscous flows. The convergence rate of the modified multigrid code for obtaining steady-state solutions of high Reynolds number viscous flows in the supersonic/hypersonic flow regimes (up to Mach 6), is comparable to the convergence rate in transonic flows. Convergence histories and detailed comparisons with the experimental data are presented for two problems of practical interest. Based on these solutions, it is concluded that the resulting code is capable of predicting high-speed viscous-flow problems in an efficient and reliable manner.

ACKNOWLEDGMENTS

The authors are deeply indebted to Mr. Peter Covell and Ms. Gloria Hernandez of NASA Langley for making some of their unpublished data for HSCT available for this study; to Ms. Mary Adams for her invaluable help in producing the flow visualization graphics used in this paper and to Mr. John Stewart for the grid generation for the conical frustum case.

REFERENCES

1. K. Sawada and S. Takanashi, 'A numerical investigation on wing/nacelle interferences of USB configurations', *AIAA Paper 87-0455*, 1987.
2. A. Jameson and T. J. Baker, 'Multigrid solution of the Euler equations for aircraft configurations', *AIAA Paper 84-0093*, 1984.
3. A. Jameson and T. J. Baker, 'Improvements to the aircraft Euler method', *AIAA Paper 87-0452*, 1987.
4. N. J. Yu, K. Kusunose, H. C. Chen and D. M. Summerfield, 'Flow simulations for a complex airplane configuration using Euler equations', *AIAA Paper 87-0454*, 1987.
5. R. K. Agarwal and J. E. Deese, 'Computation of transonic viscous airfoil, inlet, and wing flowfields', *AIAA Paper 84-1551*, 1984.
6. U. Kaynak and J. Flores, 'Advances in the computation of transonic separated flows over finite wings', *AIAA Paper 87-1195*, 1987.
7. V. N. Vatsa, B. W. Wedan and E. Turkel, '3-D Euler and Navier–Stokes calculations for aircraft components', *NASA CP-3020*, 1989, pp. 571–580.
8. J. L. Thomas, S. T. Krist and W. K. Anderson, 'Navier–Stokes computations of vortical flows over low-aspect-ratio wings', *AIAA J.* **28**, 205–212 (1990).
9. V. N. Vatsa and B. W. Wedan, 'Development of a multigrid code for 3-D Navier–Stokes equations and its application to a grid-refinement study', *Comput. Fluids*, **18**, 391–403 (1990).
10. N. Decker and E. Turkel, 'Multigrid for hypersonic inviscid flows', in B. Engquist and B. Gustafsson (eds), Proc. Int. Conf. hyperbolic problems, Chartwell-Bratt, Bromley, Kent, 1990, pp. 285–299.
11. A. Jameson, W. Schmidt and E. Turkel, 'Numerical solutions of the Euler equations by finite volume methods using Runge–Kutta time-stepping schemes', *AIAA Paper 81-1259*, 1981.
12. A. Jameson and T. J. Baker, 'Solution of the Euler equations for complex configurations', *AIAA Paper 83-1929*, 1983.
13. A. Jameson, 'Solution of the Euler equations by a multigrid method', *Appl. Math. Comput.*, **13**, 327–356 (1983).
14. E. Turkel, R. C. Swanson, V. N. Vatsa and J. W. White, 'Multigrid for hypersonic viscous two- and three-dimensional flows', *AIAA Paper 91-1572*, 1991.
15. P. Jorgenson and E. Turkel, 'Central difference TVD and TVB schemes for time dependent and steady state problems', *AIAA Paper 92-0053*, 1992.

16. S. Abarbanel and D. Gottlieb, 'Optimal time splitting for two- and three-dimensional Navier–Stokes equations with mixed derivatives', *J. Comput. Phys.*, **41**, 1–33 (1981).
17. A. Brandt, 'Multi-level adaptive solutions to boundary-value problems', *Math. Comput.* **31**, 333–390 (1977).
18. G. C. Ashby, Jr. and W. F. Staylor, 'Aerodynamic characteristics of a modified cone-conical-frustum entry configuration at Mach 6·0', *NASA TN d-4598*, 1968.
19. A. W. Robins, S. M. Dollyhigh, F. L. Beissner, K. Geiselhart, G. L. Martin, E. W. Shields, E. E. Swanson, P. G. Coen and S. J. Morris, 'Conceptual development of a Mach 3·0 high-speed civil transport', *NASA TM-4058*, 1988.
20. P. Covell, G. Hernandez and J. Flamm, 'Supersonic aerodynamic characteristics of a Mach 3 high-speed civil transport configuration', *AIAA Paper 90-3210*, 1990.
21. R. W. Newsome and M. S. Adams, 'Numerical simulation of vortical-flow over an elliptical-body missile at high angles of attack', *AIAA Paper 86-0559*, 1986.